https://doi.org/10.1016/j.msea.2017.02.056

Excellent combination of strength and ductility in 15Cr-2Ni duplex stainless steel based on ultrafine-grained austenite phase

Jianquan Wan, Haihui Ruan*, Sanqiang Shi

Department of Mechanical Engineering, The Hong Kong Polytechnic University, Hung Hom, Kowloon, Hong Kong, China

Abstract

The room-temperature duplex structure of duplex stainless steel is always metastable, which suggests that non-equilibrium phase transformation can be further exploited for producing duplex stainless steel having the same chemical compositions and phase constitution but different microstructures. This work uses rapid solidification obtained duplex stainless steel to expand heat-treatment temperature range to achieve 50/50 duplex structure. Research shows an equilibrium state for the phase constitution of duplex stainless steel after sufficient long time annealing, and establishes the non-equilibrium kinetics diagram of ferrite-to-austenite transition in cold-rolled duplex stainless steel. Duplex stainless steel samples with about 50% austenite phase were prepared using different non-equilibrium thermal process and exhibit disparate strength and ductility. The sample, which exhibits optimum mechanic property, is attributed to the bimodal distribution of austenite grain size.

Key words: Duplex stainless steel; Plastic deformation; Thermodynamics and kinetics of processes in materials; Mechanical property; Bimodal size microstructure

* Corresponding author: Tel./fax: + 852 2766 6648.

E-mail address: haihui.ruan@polyu.edu.hk (Haihui Ruan).

1. Introduction

Duplex stainless steel (DSS) attracts wide attention in recent years owing to its excellent combination of strength, ductility and corrosion resistance. DSS exhibits at least twice the yield strength, and similar or higher corrosion resistance of their austenitic counterparts, and has been widely used in many stringent environment such as oil, petro-chemical and desalination service [1-6].

The early development of DSS was to increase the fraction of ferrite phase through adjusting the ratio of chromium and nickel content on the basis of the well-known 18-8 ASS. Therefore the chromium and nickel contents in most DSSs are in the ranges of 18~23 % and 4~7 %, respectively. However, chromium and nickel are not only high-cost materials but also strategic resources for many critical applications such as turbine engines or nuclear power plants [7]. In order to minimize both chromium and nickel content in the general-purpose stainless steel, efforts are made to partially replace Cr and Ni respectively with Al and Mn or other equivalent elements [8] or to develop new stainless steel based on Fe-Mn-Al system [9-13]. In general, the design of chemical composition can be guided by the phase prediction diagrams, which was pioneered by Schaeffler [14], Hull [15] and DeLong [16] and now standardized by the US-based Welding Research Council (WRC) [17].

Developing DSSs based on the quinary Fe-Cr-Ni-Al-Mn system is intricate since the properties and phase constitution are affected by not only the chemical composition but also the thermal and mechanical treatments. The phase predication

diagram based on the products of welding can only provide very limited guidance sine the thermal process for producing DSS is significantly different from welding. The usual synthesis process of DSS, after the alloy is cast, involves forging for remove internal voids, isothermal holding for adjusting the phase composition and final quenching to retain the high-temperature microstructure. In this process, the equilibrium phase diagram may help to choose an appropriate holding temperature [1]. But detailed effects of annealing temperature and time, cooling rate and plastic deformation cannot be found in a phase diagram, which therefore limits the choices of process parameters. For this purpose, the complete picture of non-equilibrium phase transformation shall be established.

It is well known that rolling leads to “pancake” grains, which is an effective approach to obtain small grains in the process involving phase transformation, since nucleation of new phase preferably starts at grain boundaries and the pancake-shaped grains limited the space of grain growth.

The process combining plastic deformation and annealing is a widely adopted approach to produce ultrafine grains [18]. DSS heat-treated at low temperature can not only reduce growth rate of grains but also keep more deformed and dislocated microstructures, leading to finer austenite grains [19]. This work was motivated by the question how to optimize the mechanical property of DSS in production. Therefore, the recently-developed 15Cr-2Ni DSS with approximately 50% ferrite/austenite phase was produced in different approaches to demonstrate disparate combinations of strength and ductility, once the non-equilibrium phase

transformation of 15Cr-2Ni DSS was well described. With our prior knowledge of resource-saving DSS [8], 15Cr-2Al-2Ni-11Mn was chosen as the model materials.

2. Experimental

The raw materials were melted in an electric arc furnace and then fast solidified into a copper mould at room temperature, which resulted in about 70% ferrite phase in the as-cast alloy. The resulted chemical composition of the as-cast alloy is obtained through spectroscopic analysis and shown in Table 1. Cold-rolled (70% thickness reduction) samples were annealed at a temperature T for some time t and finally cooled to room temperature. The ranges of T and t are 750~1250 °C and 1~240 min, respectively. All samples were electrolytically etched in 15 wt.% KOH solution, which makes the austenite bright and the ferrite grey under an optical microscope. The phase constituent of a sample is estimated from ten optical images obtained from the etched surface using a 200x objective lens. The average of 10 measurements on each sample was taken as the volume fraction of austenite phase. All samples were cut from the same depth of the ingot to minimize the effect of inhomogeneity. The centre region of each heat-treated sample was examined to avoid any boundary effects.

For tensile test, all samples were wire-cut into dog-bone shape with the gauge dimension of 5×30×1 mm, to which a 25-mm extensometer can be attached for an accurate measurement of the elongation. Micrographs on the fracture surface of samples after tensile test were observed in a Jeol 6490 scanning electron microscope

(SEM). Selected samples were subjected to investigation using transmission electron microscope (TEM, JEOL 2000FX working at 200 kV). The sample was thinned into 30 μm by sand paper, punched into wafers of 3 mm diameter and ion milled to get the TEM foils. The Vickers indentations were performed with a load of 250 mN during 10s. For each sample, a minimum of 10 indentations were performed. Nano-indentation is performed with Berkovich tip using load-control process with the maximum load 8000 μN, loading rate 1600 μN/s and dwell time 2 seconds.

3. Results

3.1 Microstructure

Fig. 1(a) and Fig. 1(b) show the typical optical microstructures of the DSS specimens, with annealing temperature at 1050 °C for 30 min followed by water quenching and air cooling, respectively. The matrix shows an obvious duplex structure of austenite (γ) and ferrite (δ). The bright etched austenite islands were embedded in grey etched ferrite matrix and no secondary precipitates were found in the ferrite–ferrite and ferrite–austenite phase boundaries. The above metallographic results were further confirmed by XRD as shown in Fig. 2. The volume fraction of austenite phase increases as the cooling rate reduces from water quenching to air cooling, which is also exhibited in terms of the change of the relative height of the peaks pertaining to the $\gamma(111)$ and $\delta(110)$ planes.

3.2 Non-equilibrium kinetics diagram based on water quenched samples

The detailed temperature-time dependent result of austenite constituent ϕ_γ based on

the cold-rolled DSS is shown in Fig.3, which is obtained by isothermal holding followed by water quenching. Austenite volume fraction increases with annealing time and then does not change any more after sufficient long annealing time, so an equilibrium state was concluded to be existed for a specific DSS at a definite annealing temperature. The phase constitution was gradually diffusion-transformed to the equilibrium state with annealing time, and the transformation rate increases with annealing temperature. The experimental data are closely fitted using Avrami equation [20, 21]:

$$\phi_\gamma / \phi_\gamma^e = 1 - \exp(-((t + t_0)/\tau)^n), \quad (1)$$

where ϕ_γ^e is the volume fraction of austenite phase at the equilibrium state, t_0, n and τ are fitting parameters. For $t_{0,}$ it is an assumption for the samples before heat treatment already contained about 30% austenite phase. The magnitudes of fitting parameters n, τ, t_0, ϕ_γ^e are listed in Table 2. For $n \approx 2.5$ in the fitting result, it is also consistent with the kinetics of σ phase precipitation in [29, 30], which is also a diffusion meditated process. Fig. 4 shows the experimental results and fitting curves on the temperature-time dependent variation of austenite content, which exhibits the non-equilibrium kinetics and the equilibrium state of 15Cr-2Al-2Ni-11Mn alloy. For confirming the fitting, two more heat-treatments were conducted based on the fully ferritic samples obtained after annealing at 1250 °C for 30 min. The fully ferritic samples were then aged at 850 °C for 150 and 240 min, leading to the two pentagrams in Fig. 4, which are all along the curve of 850 °C. The inset shows the

microstructures of these two samples.

3.3 The accessible range of phase constitution

In the conventional synthesis approach of DSS, the melt is generally slowly cooled in furnace or air, which usually results in a small content of ferrite owing to the δ-to-γ transformation when temperature reduces. For the 15Cr-2Ni DSS, air cooling generally brings about 40% ferrite in the as-cast sample [8]. However, in this work, the quick quenching using copper mould suction is employed, which leads to the 70% ferrite in the as-cast sample. The justification for the present approach can be understood using the diagrams shown in Fig. 5.

To elaborate the design of the thermal process for adjusting the phase contrast in DSS, the equilibrium ferrite content of both cold-rolled and as-cast samples against temperature 750~1250 °C, which is approximated by water-quenched samples after sufficient long time annealing, is plotted in Fig. 5. If the pre-heated sample consists of 40% ferrite as the dashed line shown in Fig. 5(a), isothermal holding leads the ferrite content to the equilibrium magnitude and cooling reduces the content of ferrite. The shaded area in Fig. 5(a) indicates the accessible range of ferrite content through heat treatment. If the target ferrite content in the DSS is 50%, it is then apparent that the accessible temperature range of heat treatment must be larger than the intersection point (about 850 °C) between the 50% reference line and the equilibrium curve.

However, if the ferrite content of the pre-heated sample is 70%, as shown in Fig. 5(b), the additional accessible range of ferrite content is indicated as the dotted area,

in which heating leads to reduction of ferrite content. And the 50% ferrite content can be obtained easily at the low temperature range of 750~850 °C. It must be emphasised that the low-temperature thus utilized can render a very large time window for achieving different phase morphologies.

This consideration stimulates the research on comparing the mechanical performance of DSSs with about 50% ferrite content but obtained at temperature of 750 and 1000 °C respectively.

3.4 **Mechanical Properties**

The above knowledge on the effects of temperature, time and cooling method facilitates the synthesis of DSS of a desired phase constitution through different heat-treatment process. In order to exhibit the impacts of different heat-treatment process on the mechanical properties, four different processes with annealing temperature 750 °C and 1000 °C were designed, which all bring about the DSS with about 50% ferrite phase. These are cold-rolled samples treated at 1000 °C for 15 min (S1) and 30 min (S2), and at 750 °C for 90 min (S3) followed by air cooling, which results in 52%, 50%, and 49% ferrite phase, respectively. As-cast sample treated at 1000 °C for 30 min followed by air cooling (S4) was also conducted on the tensile test to show the effect of plastic deformation on the mechanic property, and its ferrite content is 52%.

Fig. 6 shows the true stress-strain and work hardening rate curves of the four samples. The true stress-strain curves, after the yield point, are well fitted using the

equation:

$$\sigma_T = \sigma_y + k\varepsilon^n , \tag{2}$$

where *k* and *n* are fitting parameters. The hardening rate is then $\frac{d\sigma_T}{d\varepsilon} = nk\varepsilon^{n-1}$, which has been shown in Fig. 6 for different samples. With the stress-strain relation, the nominal necking strain can be obtained using the Considere's criterion:

$$\left.\frac{d\sigma_T}{d\varepsilon}\right|_{necking} = \sigma_T , \tag{3}$$

which results in the end asterisks of the dashed fitting curves as shown in Fig. 6. The actual necking strain is about 70~80 % of the nominal one, which could be attributed to the internal voids resulted from casting[1]. The measured yield stresses, based on the fitting Eq. (2) or using the 0.2% proof stress, are listed in Table 3. All four samples exhibit good mechanical performance in terms of the yield strength of 306~499 MPa, ultimate tensile strength of 708~853 MPa and elongation of 20~33%. It is learned that severe plastic deformation before the heat treatment renders some constrains to the growth of austenite phase in the process of annealing, which makes the sample S2 stronger but less ductile than sample S4. Comparing S1 and S2, the ferrite content of DSS reaches the equilibrium state after annealing at 1000 °C for 15 min that can be concluded from Fig.4, so grain size grows larger for the 30 min annealing and leads to the higher ductility but lower strength of S2.

The metallographs of samples S1~S4 confirm the above description as shown in

[1] Forging can remove the internal voids and may further improve the ductility [8].

Fig. 7. Fig. 7(b) and Fig. 7(d) are very common DSS morphologies, which are the results of conventional 30 min annealing. For Fig. 7(a) and Fig. 7(b), the reduced annealing time led to many small γ phases embedded in δ matrix in S1, which explains the higher yield strength in comparison with S2. It indicates that γ phase can have bi-modal size distribution due to the growth from the new nucleus and existing ones respectively. This feature can be better controlled if the annealing temperature is reduced, as exemplified in Fig. 7(c), where a large number of even smaller γ phases are exhibited. It is noted that the yield strength of S3 is lower than that of S1 and the ductility of S3 is even larger than that of S2. This low-temperature heat treatment brings about the best combination of strength and ductility as well as the largest hardening rate at large plastic strain. S1 and S3 exhibit the best strength and ductility respectively, which is consistent with the micrograph of fracture surface. Fig. 8 exhibits the fracture surfaces of S1 and S3 using SEM. Fig. 8 (a) shows apparently brittle fracture feature of S1, while Fig. 8 (b) shows nearly all dimples feature of S3. Further research was conducted to discuss the mechanic mechanism of the contrast between S1 and S3.

4. Discussion

Heat treatment is an effective step for improving the mechanical performance of DSS. The conventional annealing temperature is around 1000 °C, mainly concerned on avoiding the secondary phase precipitation. The size and distribution of secondary phase can be controlled by adjusting the chemical composition and heat treatment, and secondary phase can be beneficial for the mechanical performance of DSS in this

condition. Therefore, low temperature heat treatment should be useful for improving the mechanical performance of DSS. In order to understand the mechanic mechanism of the contrast between S1 and S3, microhardness (FM-7E, FUTURE-TECH JAPAN) and nano-indentation tests (Hysitron) on ferrite and austenite phases were conducted. The average microhardness values of ferrite and austenite phases are 307±13 and 261 ± 5 HV respectively for S1, while 206±18 and 363±20 HV respectively for S3. Nano-indentation result in Fig.9 shows that the average hardness of ferrite and austenite phases were 3.22 ± 0.14 and 2.71 ± 0.13 GPa for S1, respectively, while 2.44 ± 0.15 and 3.54 ± 0.20 GPa for S3, respectively. In the macroscopic deformation of two-phase alloys, each phase undergoes elastic and plastic strains under the mutual constraint of the other constituent. The onset of plastic deformation of DSS should occur in the softer phase and is accompanied by severe load redistribution between ferrite and austenite phases [22, 23]. Even though some investigations have shown that austenite phase in DSS could be harder [24, 25] than the ferrite phase, the conventional notion about DSS is still that the ferrite phase is harder [26-28], which is the cause of higher yield strength of DSS than that of ASS. However, S3 renders the converse result that the austenite phase in DSS can also be the reinforcing phase. The strength of the austenite phase in S3, if estimated using Tabor's empirical conversion between hardness and strength with ratio 3.5, is about 1 GPa. Since the austenite phase can be pronouncedly hardened by plastic deformation, the hardness-strength conversion only leads to the flow stress at a large plastic strain. Based on the assumption that the incipient plasticity of S3 is merely due to yielding

of ferrite phase, the yield strength of austenite phase in S3 would be about 540 MPa considering the ratio of hardness of two phases (3.54 / 2.44). Comparing to the conventional ASS, such as 304 and 316, which have the yield strength about 200 ~ 300 MPa [29], the austenite phase in S3 is exceptionally strong.

The inset of Fig. 9 shows the partition coefficient of major alloying elements in δ and γ phases and the hardness ratio ($HR_{\gamma/\delta}$). The partition coefficient is defined by $K_i = X_i^{\gamma} / X_i^{\delta}$, where $X_i^{\gamma \text{ or } \delta}$ is the concentration of element i in γ or δ phase, estimated using the energy-dispersive X-ray spectroscopy (EDS). The as-cast sample is also listed as a reference, and its partition coefficients for all alloying elements are nearly equal to 1 due to rapid solidification. The comparison between as-cast sample, S1 and S3 indicates that low-temperature treatment leads to notable increase of nickel and manganese and decrease of aluminum in the austenite phase of S3. It is known that the deformation mechanism of ASS depends strongly on the stacking fault energy (SFE). With higher SFE, cross-slip is more favored than planar slip [30, 31], leading to the higher yield strength. The empirical equations of SFE [32-36] for ASS all indicate that Ni and Mn are more prominent in increasing SFE than that of Cr. Therefore the austenite phase of S3 shall have a higher SFE than that of S1. The SFE of Al-alloyed ASS cannot be found. However, it shall be stressed that solid-solution hardening is not sufficient to explain why the austenite phase in S3 is even harder than the ferrite phase of S1.

The typical TEM test was conducted to show the grains distribution as shown in

Fig. 10. Fig. 10(a) shows the significantly elongated grains in S1, where the average length of short axis is already about 800 nm. In contrast, Fig. 10(b) shows rounded (equiaxied) grains in S3 with average size of about 750 nm. It was not found any secondary phase in S1, while one σ phase grain with diameter about 338 nm was found in S3 as shown in the inset of Fig. 10(b). However the σ phase does not induce brittleness for S3 at least in comparison with S1 and S2. The grain size indicated in Fig. 10(b) does not distinguish whether they are austenite or ferrite grains. Considering the current DSS casting with 70% ferrite content, ferrite-to-austenite transformation occurs during annealing as shown in Fig.5(b). The ferrite grains, which formed during melt quenching, should be larger than the newly formed austenite grains. Therefore, 750 nm can be regarded as the upper bound of the average size of austenite grains in S3. The small grains impart high strength owing to the Hall-Petch effect, and the bio-modal size distribution of γ phase could be the cause of the largest strain hardening rate and ductility of S3 among the four examined samples [37-39]. The yield strength of austenite phase can be estimated by substituting the average grain size 750 nm into established Hall-Petch relations for DSS [18, 40] and ASS [41-44]. The results are in the range of 559 ~ 738 MPa [18，40-44], among which the minimum magnitude 559 MPa based on [18] agrees admirably with nano-indentation result (540 MPa). Therefore, the ultra-fine grain size of the austenite phase in S3 is concluded to be the main cause of its high strength, and the optimum mechanic property of S3 could be attributed to the bimodal distribution of austenite grain size.

5. Conclusion

This work investigates the composition 15Cr-2Al-2Ni-11Mn to exhibit that a series of DSS samples with the same phase constituent but different microstructure and mechanical property by employing the non-equilibrium phase transformation of the primary phases. The main findings are:

1. There is an equilibrium state for the phase constitution of duplex stainless steel that does not change with annealing time any more.

2. Rapid solidification obtained duplex stainless steel expands heat-treatment temperature range to achieve 50/50 duplex structure.

3. The non-equilibrium kinetics diagram of ferrite-to-austenite transformation in 70% cold-rolled DSS was established.

4. Based on the non-equilibrium kinetics diagram and the effect of cooling method, DSS with about 50% ferrite phase was prepared using different non-equilibrium thermal process. It was found that the mechanical performance of DSS is optimised by plastic deformation and low temperature annealing. This solution brings about bimodal size of austenite grain, which acts as reinforcing and toughening phase and leads to an excellent combination of strength and ductility of DSS.

Above results also paves the way to further develop 15Cr-2Ni DSS with even larger yield strength and ductility, if the precipitation hardening (through aging [45]) and the transformation induced plasticity (through reducing Mn content [46]) are involved in ferrite and austenite phases respectively.

Acknowledgement

This work was supported by the Early Career Scheme (ECS) of the Hong Kong Research Grants Council (Grant No. 25200515) and the Departmental General Research Funds (G-UA2L) of Hong Kong Polytechnic University. We are grateful for the support.

Reference

[1] J.-O. Nilsson, Materials Science and Technology, 8 (1992) 685-700.

[2] I. Alvarez-Armas, Recent Patents on Mechanical Engineering, 1 (2008) 51-57.

[3] P. Sathiya, S. Aravindan, R. Soundararajan, A.N. Haq, Journal of materials science, 44 (2009) 114-121.

[4] S.-G. Wang, G.-P. Dong, Q.-H. Ma, Materials and Manufacturing Processes, 24 (2009) 1383-1388.

[5] J. Charles, Steel Research International, 79 (2008) 455-465.

[6] K.M. Lee, H.S. Cho, D.C. Choi, Journal of Alloys and Compounds, 285 (1999) 156-161.

[7] S.R. Chen, H.A. Davies, W.M. Rainforth, Acta Materialia, 47 (1999) 4555-4569.

[8] J. Wan, Q. Ran, J. Li, Y. Xu, X. Xiao, H. Yu, L. Jiang, Materials & Design, 53 (2014) 43-50.

[9] H. Huang, D. Gan, P.W. Kao, Scripta Metallurgica et Materialia, 30 (1994) 499-504.

[10] S. Sohn, B.-J. Lee, S. Lee, N. Kim, J.-H. Kwak, Acta Materialia, 61 (2013) 5050-5066.

[11] R. Rahimi, B.C. De Cooman, H. Biermann, J. Mola, Mater. Sci. Eng. A-Struct. Mater. Prop. Microstruct. Process., 618 (2014) 46-55.

[12] W.K. Choo, J.H. Kim, J.C. Yoon, Acta Materialia, 45 (1997) 4877-4885.

[13] D.W. Suh, S.J. Park, T.H. Lee, C.S. Oh, S.J. Kim, Metallurgical and Materials Transactions A: Physical Metallurgy and Materials Science, 41 (2010) 397-408.

[14] A.L. Schaeffler, Metal Progress, 56 (1949) 680-680 B.

[15] F. Hull, Welding journal, 52 (1973) 193.

[16] W.T. Delong, Welding journal, 53 (1974) 273s-286s.

[17] D. Kotecki, T. Siewert, Welding Journal, 71 (1992) 171-178.

[18] L. Chen, F. Yuan, P. Jiang, J. Xie, X. Wu, Materials Science and Engineering: A, 618 (2014) 563-571.

[19] T. Maki, T. Furuhara, K. Tsuzaki, ISIJ international, 41 (2001) 571-579.

[20] J.W. Christian, The Theory of Transformations in Metals and Alloys Ediz 2. an Advanced Textbook in Physical Metallurgy Parte 1. Equilibrium and General Kinetic Theory, Pergamon Press, 1975.

[21] R. Magnabosco, Materials Research, 12 (2009) 321-327.

[22] M.T. Hutchings, P.J. Withers, T.M. Holden, T. Lorentzen, Introduction to the characterization of residual stress by neutron diffraction, CRC press, 2005.

[23] M. Daymond, M. Bourke, R. Von Dreele, B.r. Clausen, T. Lorentzen, Journal of Applied Physics, 82 (1997) 1554-1562.

[24] J.J. Moverare, M. Oden, Metallurgical and Materials Transactions A, 33 (2002) 57-71.

[25] T.-H. Lee, H.-Y. Ha, J.-Y. Kang, B. Hwang, W. Woo, E. Shin, Scripta Materialia, 67 (2012) 141-144.

[26] S. Harjo, Y. Tomota, P. Lukáš, D. Neov, M. Vrana, P. Mikula, M. Ono, Acta materialia, 49 (2001) 2471-2479.

[27] N. Jia, R.L. Peng, D. Brown, B. Clausen, Y. Wang, Metallurgical and Materials Transactions A, 39 (2008) 3134-3140.

[28] E.-Y. Guo, H.-X. Xie, S.S. Singh, A. Kirubanandham, T. Jing, N. Chawla, Materials Science and Engineering: A, 598 (2014) 98-105.

[29] A. Chen, H. Ruan, J. Wang, H. Chan, Q. Wang, Q. Li, J. Lu, Acta materialia, 59 (2011) 3697-3709.

[30] C. San Marchi, B. Somerday, X. Tang, G. Schiroky, International Journal of Hydrogen Energy, 33 (2008) 889-904.

[31] M. Martin, S. Weber, W. Theisen, T. Michler, J. Naumann, International Journal of Hydrogen Energy, 38 (2013) 5989-6001.

[32] R. Schramm, R. Reed, Metallurgical Transactions A, 6 (1975) 1345-1351.
[33] C.G. Rhodes, A.W. Thompson, Metallurgical Transactions A, 8 (1977) 1901-1906.
[34] P. Brofman, G. Ansell, Metallurgical and Materials Transactions A, 9 (1978) 879-880.
[35] T. Yonezawa, K. Suzuki, S. Ooki, A. Hashimoto, Metallurgical and Materials Transactions A, 44 (2013) 5884-5896.
[36] S. Curtze, V.T. Kuokkala, A. Oikari, J. Talonen, H. Hänninen, Acta Materialia, 59 (2011) 1068-1076.
[37] Y. Wang, M. Chen, F. Zhou, E. Ma, Nature, 419 (2002) 912-915.
[38] U. Andrade, M. Meyers, K. Vecchio, A.H. Chokshi, Acta metallurgica et materialia, 42 (1994) 3183-3195.
[39] C. Youngdahl, J. Weertman, R. Hugo, H. Kung, Scripta Materialia, 44 (2001) 1475-1478.
[40] Z. Fan, P. Tsakiropoulos, P. Smith, A. Miodownik, Philosophical Magazine A, 67 (1993) 515-531.
[41] X. Chen, J. Lu, L. Lu, K. Lu, Scripta Materialia, 52 (2005) 1039-1044.
[42] S. Rajasekhara, P. Ferreira, L. Karjalainen, A. Kyröläinen, Metallurgical and Materials Transactions A, 38 (2007) 1202-1210.
[43] A. Di Schino, J. Kenny, Materials Letters, 57 (2003) 3182-3185.
[44] M. Shirdel, H. Mirzadeh, M.H. Parsa, Advanced Engineering Materials, 17 (2015) 1226-1233.
[45] R. Silva, L.F.S. Baroni, M.B.R. Silva, C.R.M. Afonso, S.E. Kuri, C.A.D. Rovere, Materials Characterization, 114 (2016) 211-217.
[46] C. Herrera, D. Ponge, D. Raabe, Acta Materialia, 59 (2011) 4653-4664.

List of Captions

Fig.8 The SEM images of fracture surfaces of samples (a) S1 and (b) S3 after tensile test

Fig.9 Load-indentation results of austenite and ferrite phases in samples S1 and S3. The dashed curves pertain to maximum and minimum hardness of a phase obtained in the tests and the solid curves are for the median hardness. The inset shows the partition factors of alloy elements and hardness ratios of as-cast sample and samples S1 and S3.

Fig.10 Bright-field TEM images showing multiple grains of samples (a) S1 and (b) S3, where segments d_0, d_1, and d_2 are 4.79, 7.89, and 5.45 μm respectively, which are used to estimate grain sizes. The inset in (b) shows duplex microstructure of S3 and a σ grain resulted from low-temperature annealing.

Figure(s)

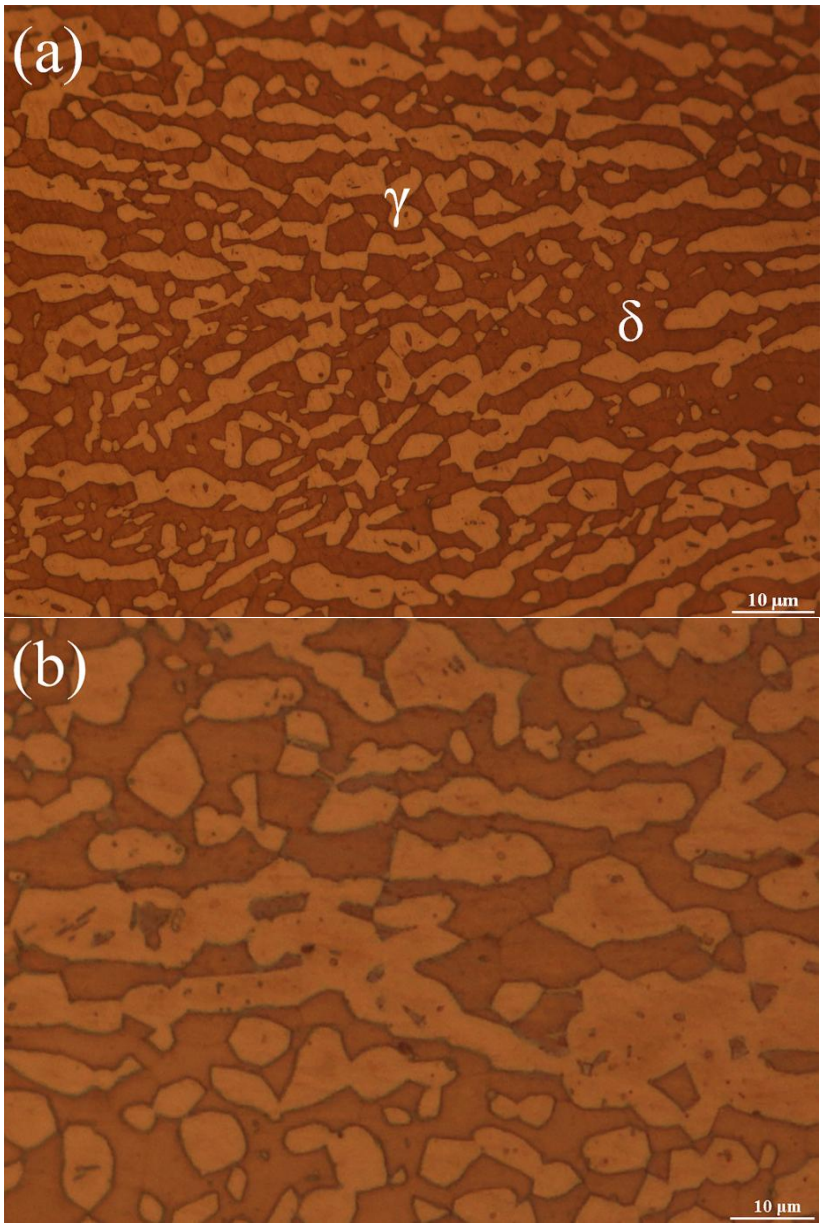

Fig.1 Metallographs of DSS samples solution-treated at 1050 °C for 30 min followed by (a) water quenching (b) air cooling

Figure(s)

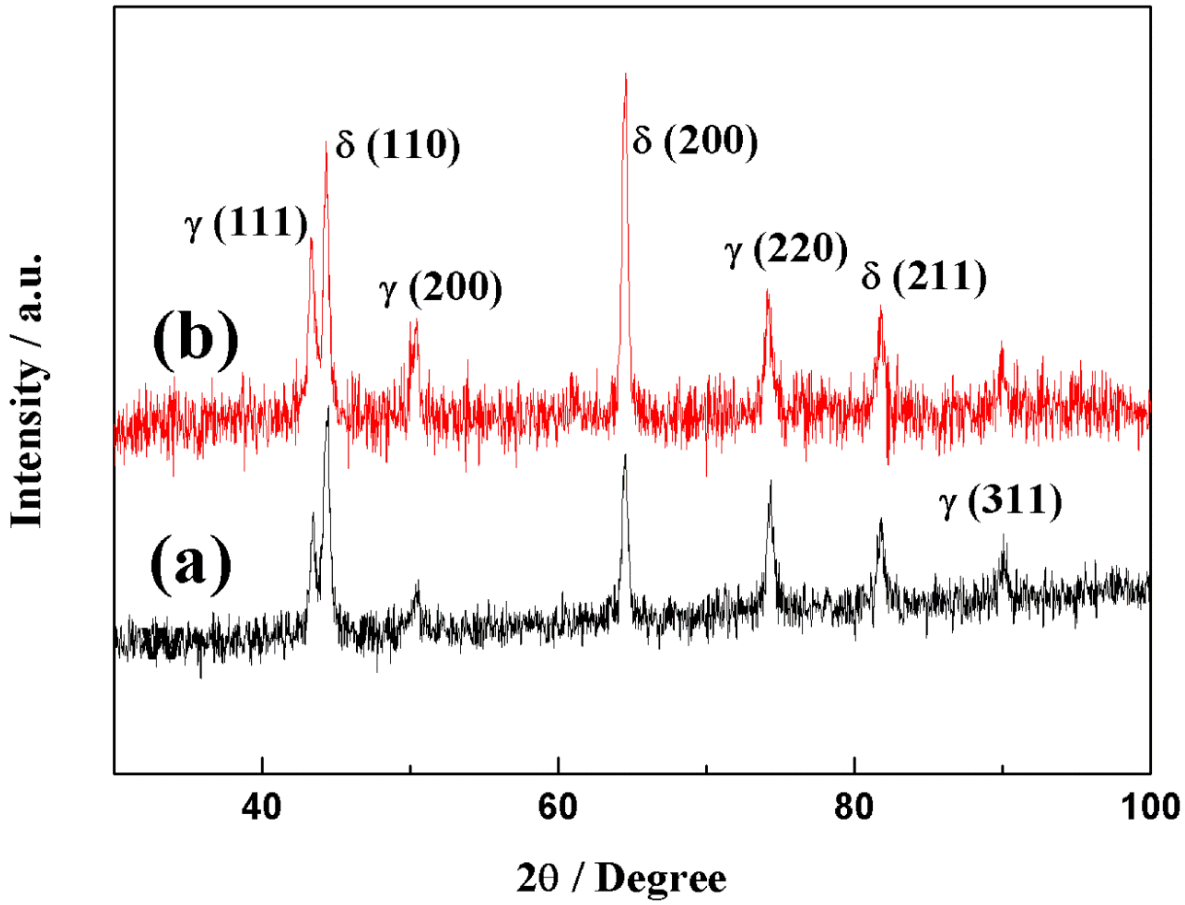

Fig.2 X-ray diffraction analysis of DSS samples solution-treated at 1050 °C for 30 min followed by (a) water quenching (b) air cooling

Figure(s)

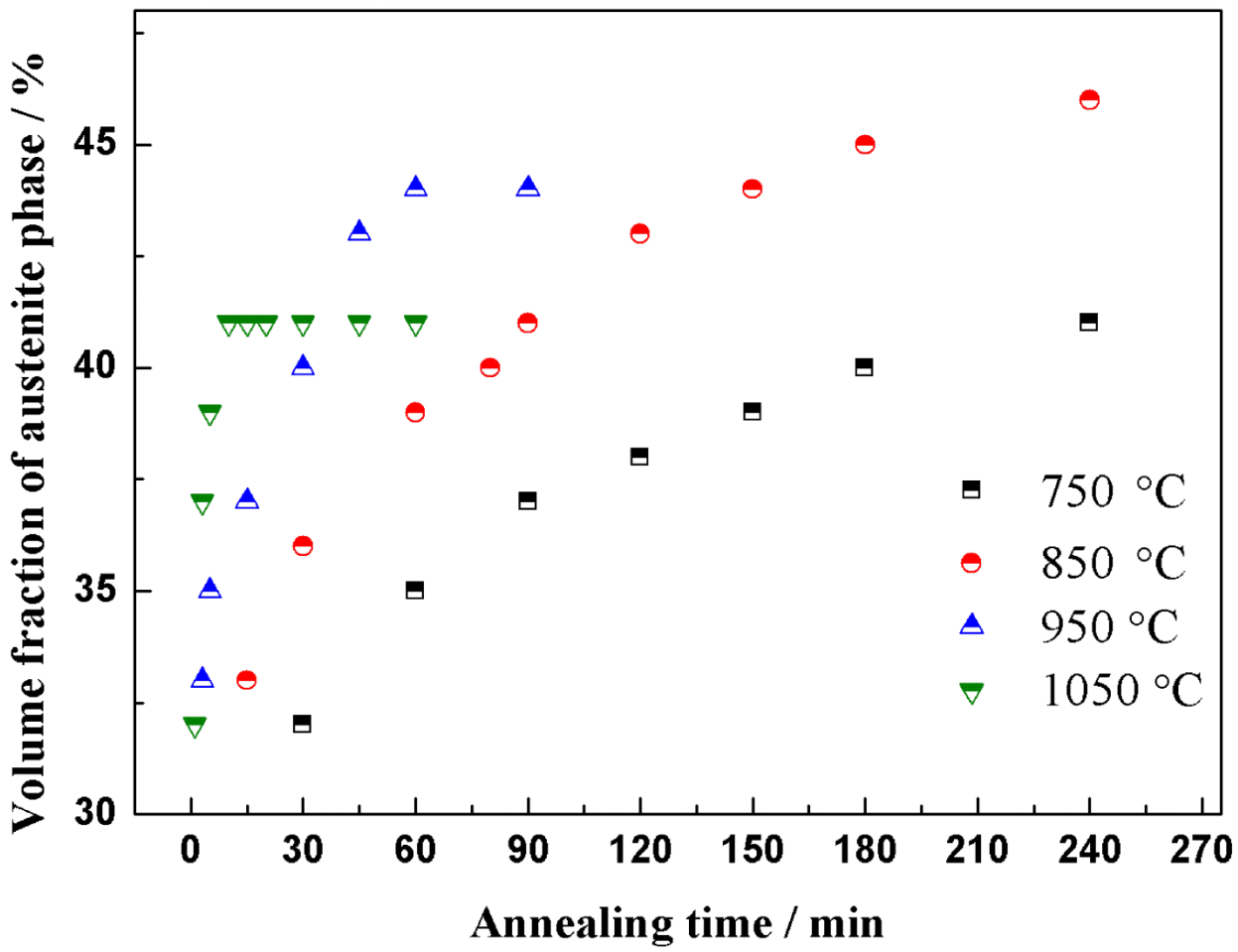

Fig.3 The detailed temperature-time dependent result of austenite content of DSS

Figure(s)

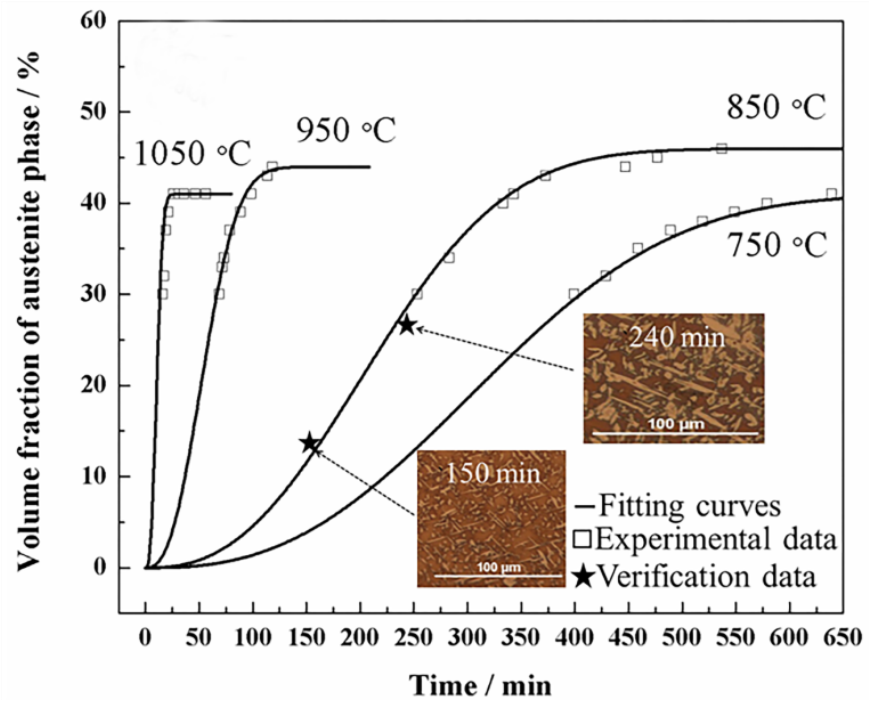

Fig. 4 Experimental results and fitting curves on the temperature-time dependent variation of austenite content, which are plotted in proportional-scale diagrams. For confirming the fitting, heat treatment based on fully ferritic sample was also conducted, leading to the additional two points and the corresponding two optical micrographs after aging at 850 °C for 150 and 240 minutes followed by water quenching.

Figure(s)

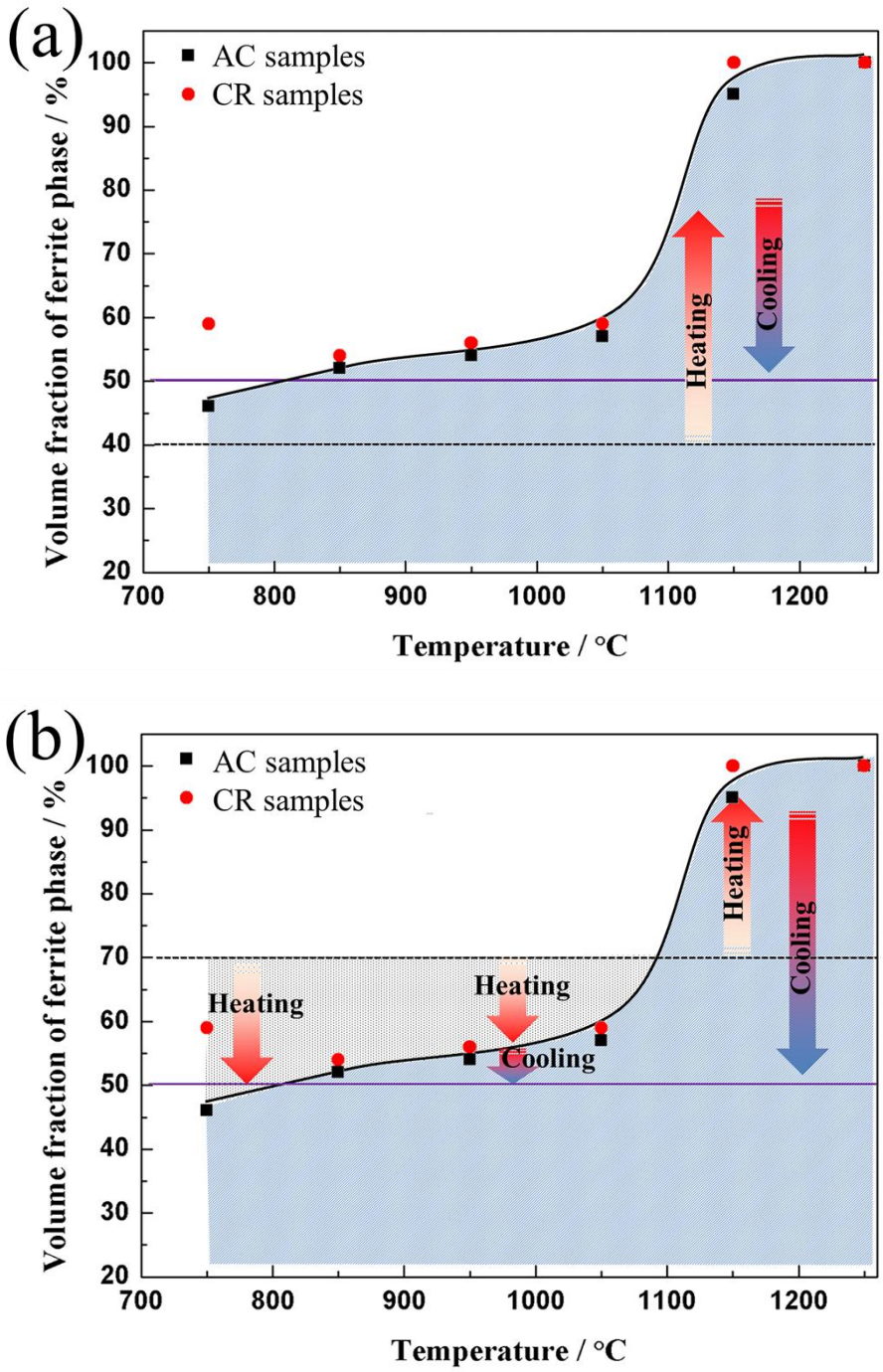

Fig.5 Schematics on accessible range of heat treatment for DSS with ferrite content of (a) 40% and (b) 70%

Figure(s)

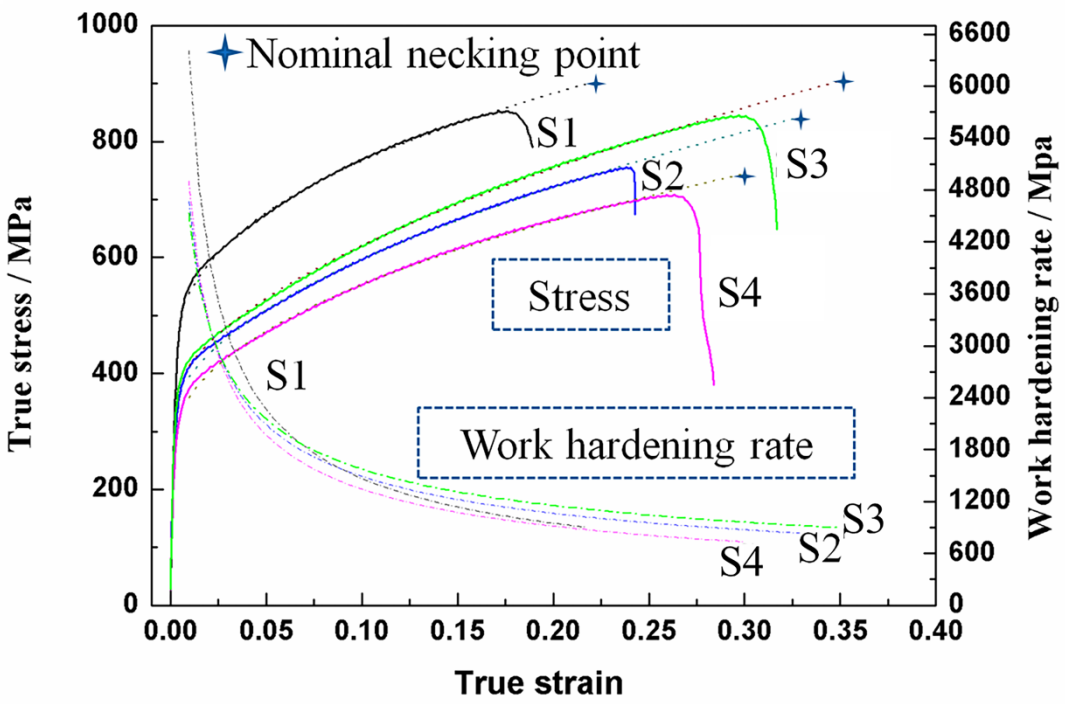

Fig.6 True stress-strain and hardening rate curves of DSS samples S1~S4

Figure(s)

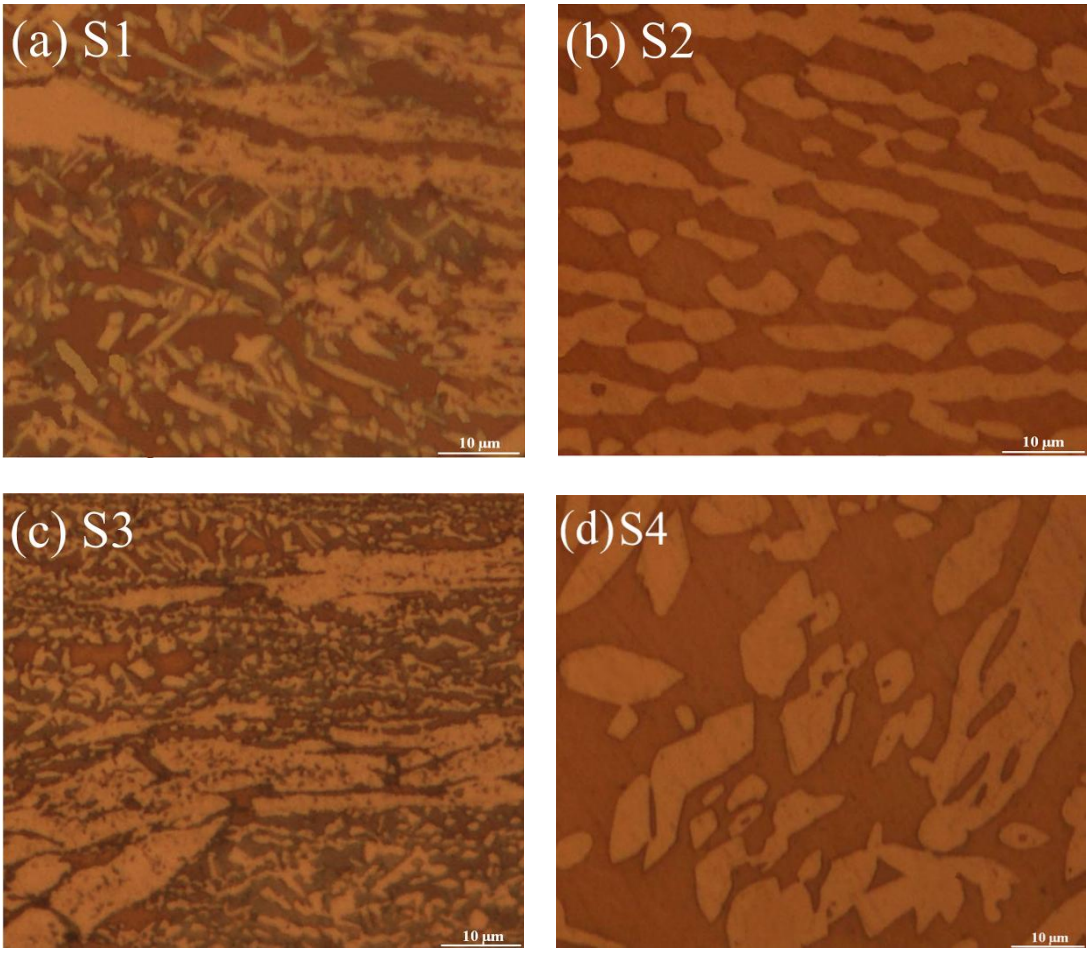

Fig.7 Metallographs of samples S1~S4

Figure(s)

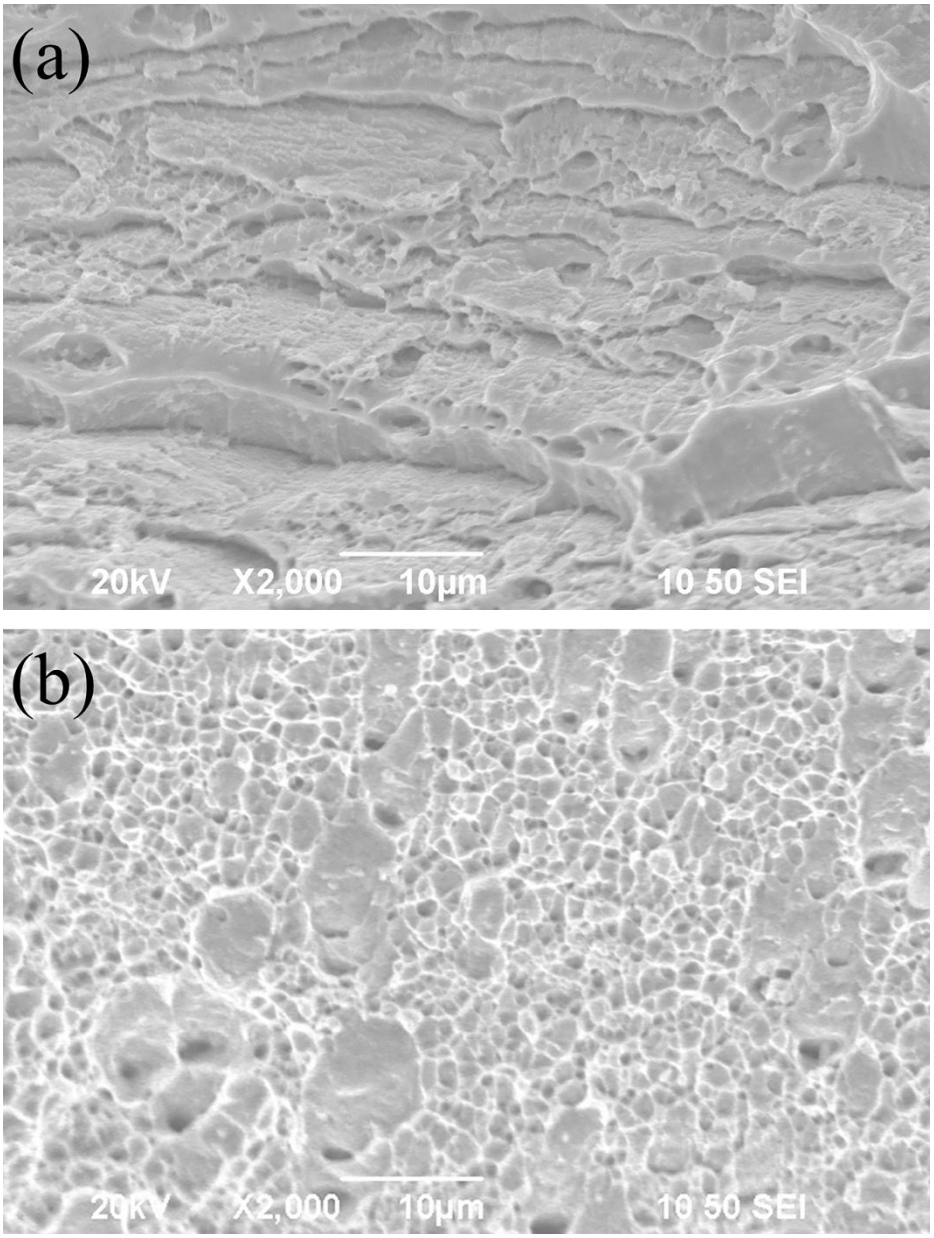

Fig.8 The SEM images of fracture surfaces of samples (a) S1 and (b) S3 after tensile test

Figure(s)

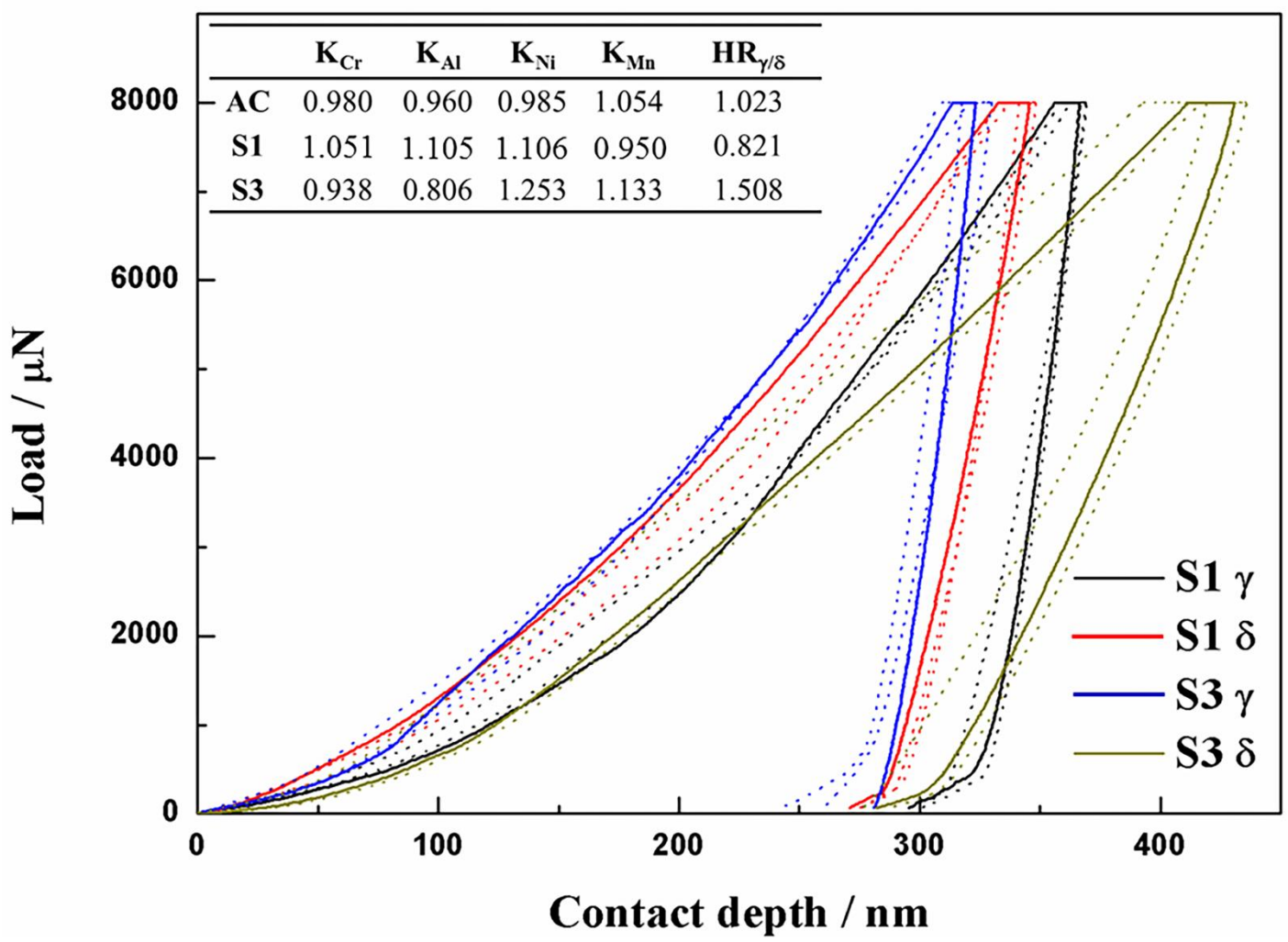

Fig.9 Load-indentation results of austenite and ferrite phases in samples S1 and S3. The dashed curves pertain to maximum and minimum hardness of a phase obtained in the tests and the solid curves are for the median hardness. The inset shows the partition factors of alloy elements and hardness ratios of as-cast sample and samples S1 and S3.

Figure(s)

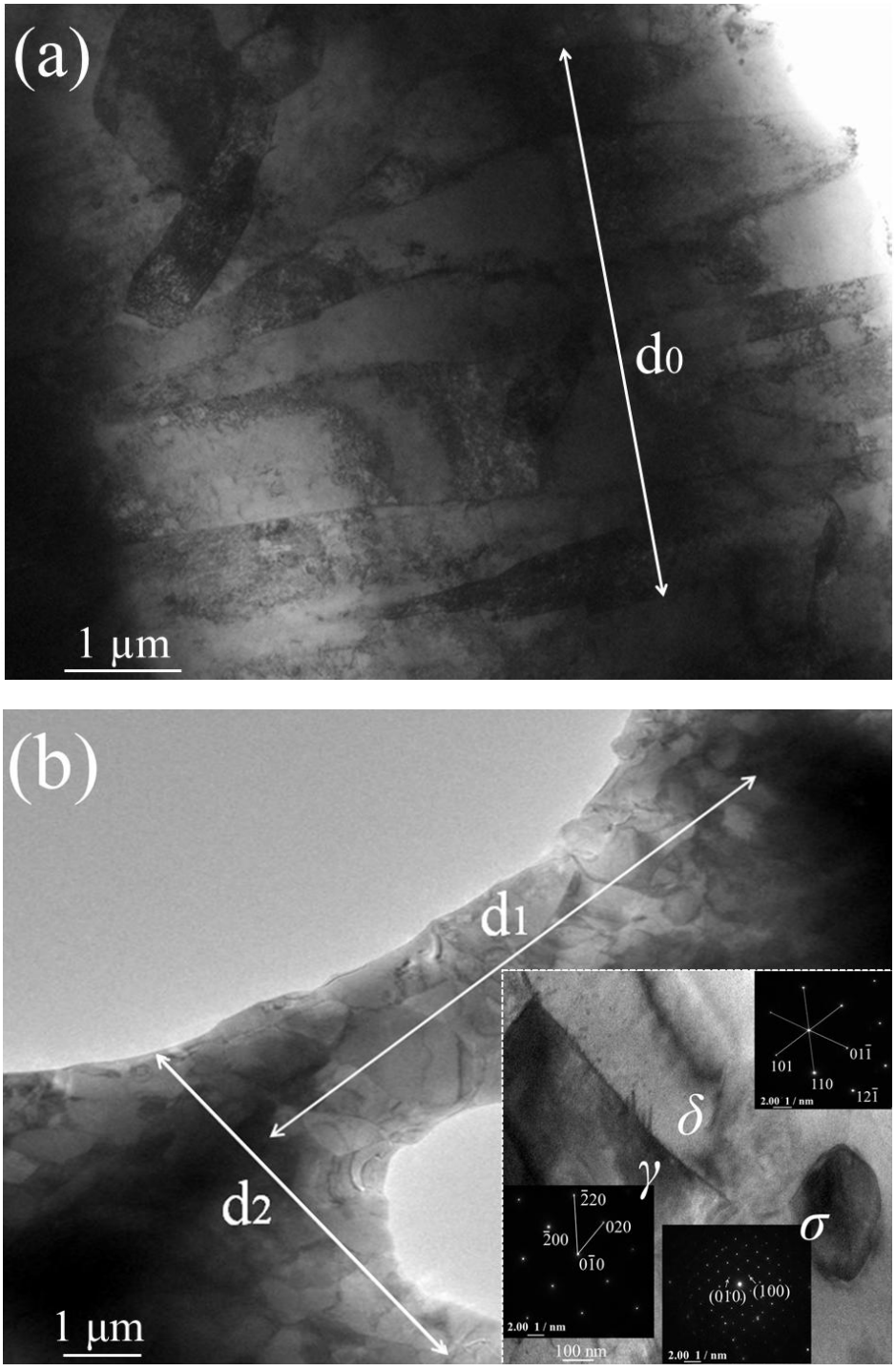

Fig.10 Bright-field TEM images showing multiple grains of samples (a) S1 and (b) S3, where segments d_0, d_1, and d_2 are 4.79, 7.89, and 5.45 μm respectively, which are used to estimate grain sizes. The inset in (b) shows duplex microstructure of S3 and a σ grain resulted from low-temperature annealing.

Table(s)

Table 1 The specific chemical compositions of 15Cr-2Ni DSS (wt.%).

Element	Fe	Cr	Al	Ni	Mn	C
Wt.%	Balance	15.27	1.96	2.04	11.05	0.02

Table(s)

Table 2 Fitting parameters of Avrami equation

T (℃)	τ (min)	n	t_0 (min)	ϕ_γ^e (%)
750	364.3	2.59	399.0	41
850	246.5	2.49	253.0	46
950	62.9	2.52	68.5	44
1050	12.0	2.69	13.2	41

Table(s)

Table 3 Mechanical property and fitting parameters for true strain of DSS samples

Samples	$\sigma_{0.2\%}$ (MPa)	σ_y (MPa)	k (MPa)	n (MPa)	Nominal necking strain	Actual necking strain
S1	499	374	928.17	0.37	0.22	0.16
S2	349	308	946.91	0.52	0.33	0.23
S3	371	335	1016.46	0.55	0.35	0.28
S4	306	255	841.23	0.45	0.30	0.24

Supplementary Material

Click here to download Supplementary Material: Research highlights.docx

► The phase constitution of DSS exists an equilibrium state after long annealing.

► Non-equilibrium kinetics diagram of cold-rolled DSS were obtained.

► Bimodal size grains were obtained by plastic deformation and low temperature annealing.

► Bimodal size grains leads to excellent mechanical performance of DSS.

Supplementary Material

Click here to download Supplementary Material: Graphical abstract.docx